AGU PUBLICATIONS

Geophysical Research Letters

The M_w 6.5 offshore Northern California earthquake of 10 January 2010: Ordinary stress drop on a high-strength fault

Meng Wei[1] and Jeffrey J. McGuire[2]

[1]Graduate School of Oceanography, University of Rhode Island, Narragansett, Rhode Island, USA, [2]Woods Hole Oceanographic Institution, Woods Hole, Massachusetts, USA

Abstract The 10 January 2010 M_w 6.5 earthquake offshore Northern California is one of the first intraplate earthquakes in oceanic lithosphere to be well captured by a GPS network. It presents an opportunity to evaluate rupture mechanics on a high-strength fault. Static inversion of the coseismic displacements shows that the slip peaks at the same depth as the expected strength envelope, where the differential stresses can be as high as 600 MPa. Laboratory experiments on peridotite predict dramatic dynamic weakening at these conditions. The observed ordinary stress drop, 2–20 MPa, may indicate that the lithosphere is much weaker than strength envelope predicts or that the failure mechanisms seen in the laboratory are not occurring during the rupture. The GPS observations show very little postseismic signal indicating that if a shear zone exists beneath the coseismic rupture, it operates at significantly greater stress levels than the coseismic stress change.

1. Introduction

Geodetic instruments have rarely observed deformation caused by intraplate earthquakes in oceanic lithosphere because they often occur far away from land-based GPS monuments. As a result, our resolution and understanding of the rupture process and overall deformation on oceanic faults is limited. The M_w 6.5 offshore Northern California earthquake of 10 January 2010 is one of the first $M > 6$ earthquakes captured by the Plate Boundary Observatory (PBO) GPS network and one of the first large earthquakes in oceanic lithosphere ever captured by a dense GPS network. Therefore, it provides an unusually good opportunity to study intraplate faults in oceanic lithosphere.

The 2010 epicenter was located about 50 km southwest of Eureka, California, in the Gorda plate, which is a microplate at the southern part of the Juan de Fuca plate and bounded by the Gorda Ridge on the west, Mendocino Fault Zone on the south, and Cascadia Subduction zone on the east (Figure 1a). This region has the highest rate of large earthquakes in the contiguous United States, having hosted more than 16 $M > 6$ earthquakes in the last 40 years. The exceptionally high rate is likely due to the strong internal deformation caused by the stress field near the triple junction where the Gorda, North American, and Pacific plates meet [*Wilson*, 1986; *Chaytor et al.*, 2004]. This high earthquake rate near a triple junction has been observed elsewhere such as the Azores triple junction at mid-Atlantic ridge [*Choy and McGarr*, 2002]. Coulomb stress interactions seem to play a role in the location and timing of earthquakes in this area [*Rollins and Stein*, 2010]. The hypocenter of the 2010 earthquake is at 29.3 km depth (U.S. Geological Survey (USGS) estimate), and hence, it ruptured a significant portion of the upper mantle beneath the oceanic crust, whose position is documented in a 3-D slab model [*Blair et al.*, 2011]. Even at the relatively young age of the Gorda plate, the stress levels in the mantle are expected to be extremely high, which is consistent with the Gorda plate producing many of the earthquakes with the highest ratios of radiated seismic energy to seismic moment (e.g., apparent stress) in global compilations [*Choy and McGarr*, 2002]. The 2010 event is one of these earthquakes that appear to have ruptured a fault at high stress levels. The USGS moment and energy estimates correspond to an apparent stress of 7 MPa (G. Choy, personal communication, 2014), which is typical for intraplate events in oceanic lithosphere of this age [*Choy and McGarr*, 2002].

In addition to recording the coseismic slip, the PBO GPS data cover the immediate postseismic interval with sufficient resolution to detect postseismic deformation. Visual inspection of the time series indicates that the postseismic deformation is relatively minor compared to the coseismic deformation (Figure 1b). This is in marked contrast to subduction zone thrust faults where the afterslip can release as much moment as the
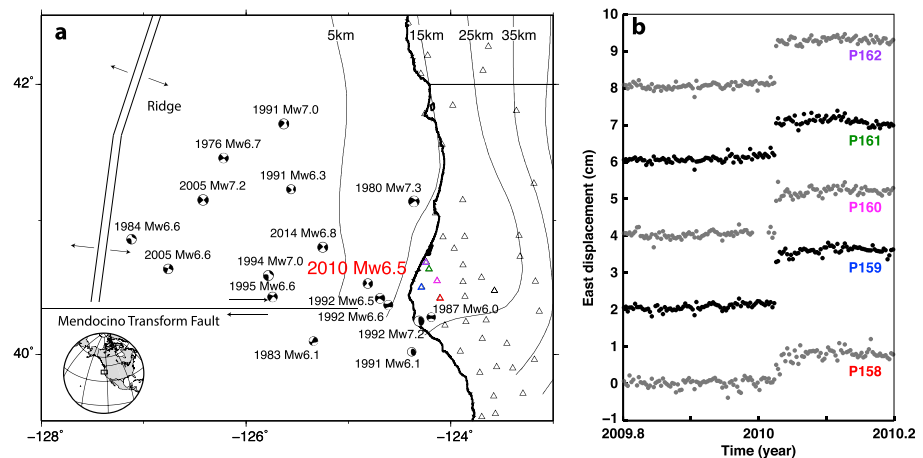
Figure 1. (a) Map near Mendocino triple junction. Thin solid lines are slab depth based on *Blair et al.* [2011]. Triangles are PBO GPS stations. Colored triangles correspond to the colored station names in Figure 1b. (b) Displacement of the east component from five GPS stations close to the epicenter of the 2010 M_w 6.5 earthquake. Secular motion has been removed.

main shock [*Hsu et al.*, 2006] and with continental strike-slip earthquakes where postseismic deformation is a clear and large signal [*Freed*, 2007]. The PBO time series provide an opportunity to study the underlying reasons for this apparent property of oceanic intraplate faults.

2. GPS Data and the Network Strain Filter

PBO level 2 GPS products were used for our analysis [*Anderson*, 2004]. These data include daily position estimates and covariance for the entire PBO network in the Stable North America Reference Frame [*Herring*, 2006]. We used 41 stations located in a 200 km by 200 km region with interstation spacing ranging from 5 to 40 km with an average of about 20 km. The closest station is about 40 km from the epicenter. Most of the PBO GPS stations in this area were installed around 2007, which allows us to estimate and remove secular plate motion. The 2010 M_w 6.5 earthquake is the first large earthquake recorded by them. There was a M_w 6.8 earthquake in 2014, which is further offshore and caused no displacement at these GPS stations.

Extracting low-amplitude coseismic and postseismic signals from a large GPS network is not a trivial task. We use the Network Strain Filter (NSF) [*Ohtani et al.*, 2010], which is a variant on the often-used Network Inversion Filter methodology [*Segall and Matthews*, 1997]. GPS time series were modeled as the summation of secular motion, transient field, site-specific noise, and seasonal noise [*Wei et al.*, 2012]. Only horizontal components were analyzed because of their higher signal-to-noise ratio. The NSF uses an extended Kalman filter to estimate all the time-varying unknowns, including the basis function coefficients of the transient field, secular motion, benchmark motion, seasonal variations, reference frame error, and a temporal smoothing parameter. We modified the process noise covariance matrix at predetermined epochs to incorporate offsets due to the coseismic deformation or the reinstallation of antennae at particular sites. An a priori state vector corresponding to zero transient slip rate is specified to initialize the filter. The extended Kalman filter updates the state vector estimate and its covariance matrix after each epoch. A back-smoothing filter is applied to determine the final optimal estimates of the state vector given the entire data time series.

The NSF results show coseismic displacements up to 1.4 cm at locations closest to the coastline, about 40 km from the epicenter, and decreased to near zero by a distance of 130 km from the epicenter (Figure 2a). The direction of movement on most stations is eastward and consistent with a single fault plane source except for station P161, which has a large southward motion. This motion was not shown in any nearby stations and therefore was treated as site-specific noise with an unclear source. Examples of the NSF results can be found in Figure S1 in the supporting information. The seasonal and site-specific noise is quite small at a level of a few millimeter. The estimate of the hyperparameter α is the best indicator of any transient deformation [*McGuire and Segall*, 2003], in this case postseismic slip. The evolution of α (Figure S2 in the supporting information) shows no jump at the time of the main shock, which indicates that no clear postseismic deformation was observed.
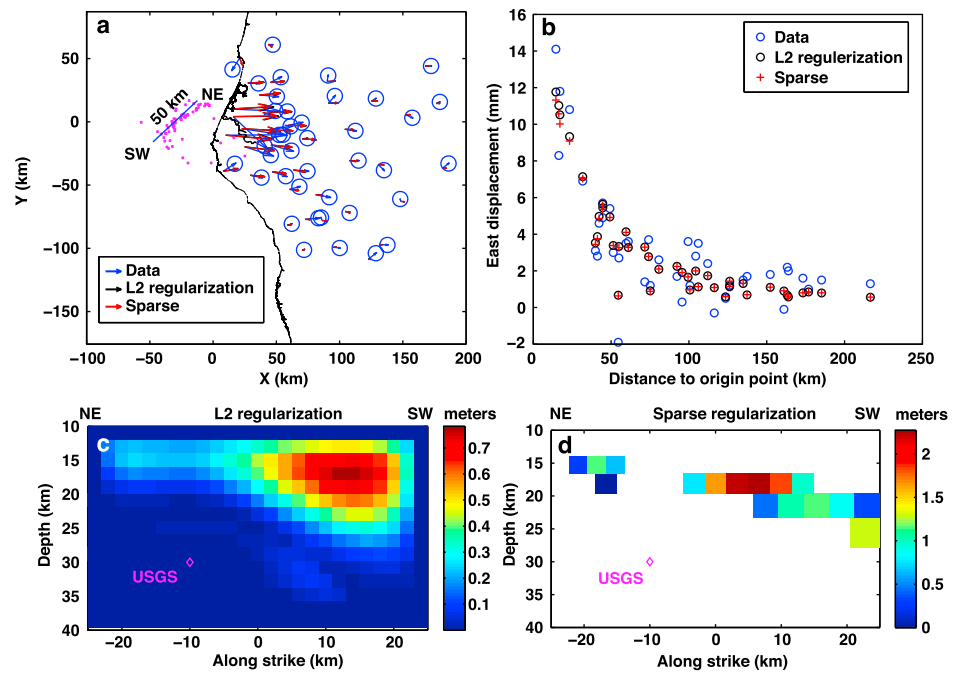
Figure 2. GPS vectors and static slip inversion models. (a) GPS data and vectors predicted by models based on L2 and sparse regularization methods. Blue solid line is the fault trace used in the inversion. Purple dots are aftershocks within a month of the main shock. Blue circles show the error of the GPS measurements. (b) Observed and predicted coseismic displacement in the east direction versus the distance from the origin point (0,0) in Figure 2a. (c) Best fitting slip model for the L2 norm regularization approach. (d) Best fitting slip model for the sparse regularization approach. The along strike coordinate is positive to the southwest.

3. Coseismic Slip Model

Coseismic displacements were modeled by slip on a planar fault in an elastic homogeneous half-space [*Okada*, 1985]. The fault geometry was determined by the locations of the main shock and aftershocks and the moment tensor solution for the main shock (strike 233° and dip 85°, http://www.globalcmt.org; Figure 2a). The distribution of GPS stations relative to the fault location limits our ability to properly resolve slip at shallow depth and at the southwest (SW) end of the fault. The main shock hypocenter was at 29.3 km depth indicating that significant slip likely occurred in the mantle. The thickness of the overriding continental plate is about 7 km including about 2 km of sediment [*Blair et al.*, 2011], which overlies the subducted oceanic crust. Hence, the subducted oceanic mantle likely corresponds to depths greater than 13 km. We limit our fault model to be 50 km long and 30 km wide (10–40 km depth). To approximate this structure, we use a uniform elastic half-space model with a constant shear modulus of 49 GPa and Lame constant of 60 GPa (average value between 10–40 km depth of the PREM model [*Dziewonski and Anderson*, 1981]).

The most common approach to invert for fault slip from surface deformation may be written as a damped least squares problem with L2 regularization: $\|Gm - d\|_2 + \alpha\|m\|_2$, where G is the Greens function, m is the slip model, d is the surface observation, and α is a nonnegative scalar [*Murray et al.*, 2001; *Fialko et al.*, 2005]. This method usually yields smooth slip models with small slip amplitude but large slip area, which can be considered to be a smooth end member. Recently, *Evans and Meade* [2012] introduced the sparse regularization approach to geodetic inversion. The problem is referred to as the least absolute shrinkage and selection operator (Lasso), min $\|Gm - d\|_2$ subject to $\|m\|_1 \leq \tau$, where τ is a nonnegative scalar that controls the sparseness of the solution. Slip models based on this method may be considered as an alternative (rough) representation to the smoothing (L2) regularized solutions. We used both methods to find the best slip models and expect that the true slip is likely somewhere between the two models.

Best fitting models for the sparse and L2 regularization methods are shown in Figure 2. The nonnegative scalar in both methods was chosen using cross-validation [*Murray et al.*, 2001] (Figure S3–S6 in the supporting
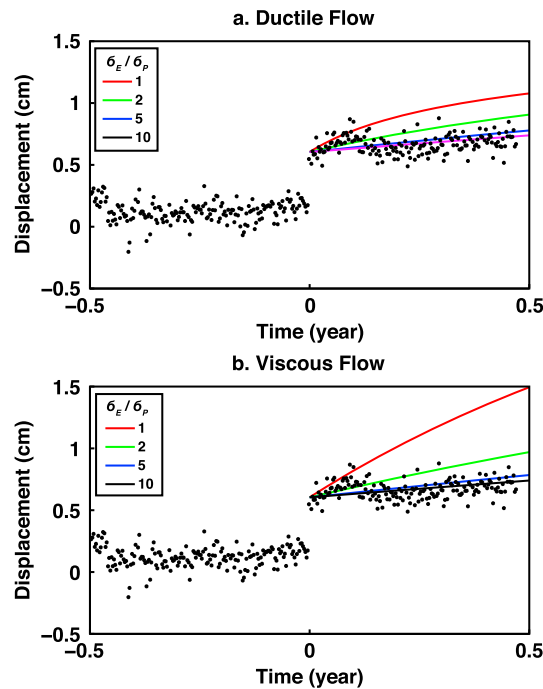
Figure 3. Forward modeling of the postseismic slip in a shear zone below the seismogenic zone. (a) Assuming ductile flow in the shear zone (e.g., $n = 3.5$). Black dots are the east component of GPS data for station P166. Colored lines are forward modeling based on *Montési* [2004]. Different colors show different ratio between σ_E, the earthquake-induced stress change on the shear zone, and σ_P, the stress required for steady state creep at the tectonic loading rate. (b) Similar to Figure 3a but for a viscous shear zone model ($n = 1$).

information). The misfit of sparse and L2 models is 1.16 and 1.14 mm, respectively. The L2 model has a rupture area of 10×25 km with an average slip of 0.5 m, and the sparse model has a rupture area of similar size but with more concentrated patches with an average slip of 1 m. Both models have a M_w of 6.51, which is consistent with the seismic estimates. The sparse model has some nonzero slip patches at the SW end, which might be artifacts of the inversion because they are farthest from GPS stations. Nevertheless, both inversions share some common features: unilateral rupture to SW of the hypocenter, maximum slip at 15–20 km depth, and no significant slip below 30 km.

We calculated the static stress changes from the slip distribution following the method of *Ripperger and Mai* [2004] and used it to constrain the stress perturbation to the region below the seismogenic zone. For L2 inversion, the maximum static stress change is about 2 MPa and the perturbation in the region below the seismogenic zone is about 1 MPa stress increase (Figure S7 in the 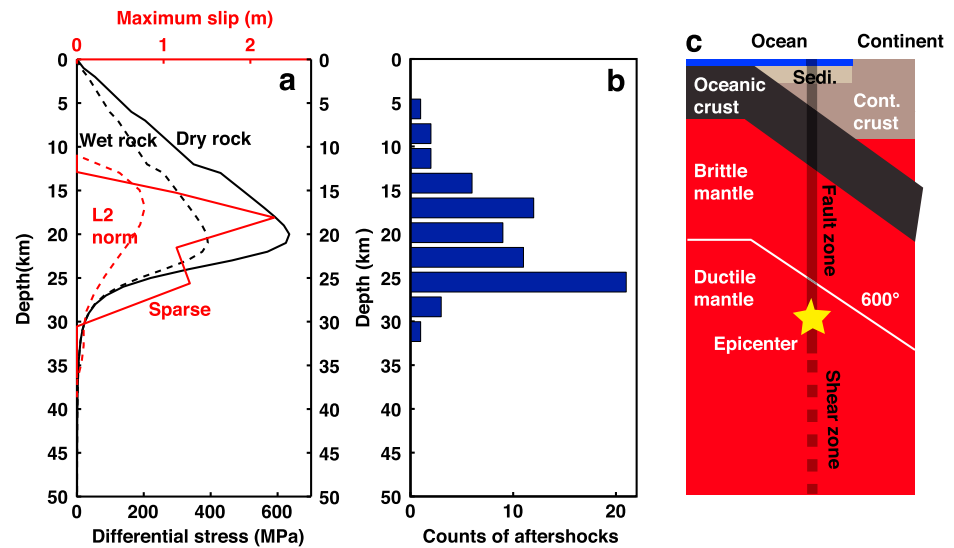supporting information). For the sparse inversion, the maximum static stress change is about 40 MPa and the average within the high slip zone is about 20 MPa. The stress perturbation in the region below the seismogenic zone is about 5–10 MPa (Figure S8 in the supporting information). We favor the higher values of stress drop, ~20 MPa, resulting from the sparse inversion because of the physical constraint that the apparent stress (~7 MPa) be less than the static stress drop [*Savage and Wood*, 1971; *Beeler et al.*, 2003].

4. Postseismic Deformation

The NSF results also yield an estimate of the postseismic deformation, but the estimated amplitudes of this transient term are extremely small (Figure S1 in the supporting information). The lack of a postseismic signal could be due to either a lack of a shear zone beneath the fault or that the ambient stress in the shear zone is large enough that the few MPa increase due to the earthquake caused a negligible change in strain rate. Following *Montési* [2004], we forward model the postseismic slip for both a ductile creep and a viscous flow rheology. For both rheologies, the ratio of postseismic velocity to the steady state velocity is related to the ratio of the coseismic stress perturbation to the stress for steady creep at the tectonic loading rate as $\frac{V_p}{V_0} = \left(\frac{\sigma_E}{\sigma_P} + 1\right)^{1/n}$, where $n > 1$ for ductile creep and $n = 1$ for viscous flow, V_p is the shear zone velocity at steady state, V_0 is the shear zone velocity immediately after the earthquake, σ_E is the earthquake-induced stress change on the shear zone, and σ_P is the stress required for steady state creep at the tectonic loading rate. The earthquake perturbation is estimated based on the static inversions (~1 MPa for L2 and 5–10 MPa for sparse). We vary σ_P, therefore, the ratio of σ_E/σ_P to generate different postseismic slip histories. The exact equations for generating postseismic slip can be found in Table 1 of *Montési* [2004]. V_p of 1 cm/yr is assumed, which is probably an upper limit. A Green's function coefficient of 0.2, which is appropriate for slip at 30 km depth and the coastal stations 40 km away, is used to project slip in the shear zone to the GPS stations.

Figure 4. (a) Strength envelope for 10 million year old oceanic lithosphere and the maximum slip versus depth for model 2. The black solid line is the strength envelope for strike-slip faults that is calculated following the Byerlee's frictional rule for dry case (equation (7b) in *Zoback and Townend*, [2001], 0.6 friction coefficient, $\lambda = 0$, where λ is the ratio of pore pressure to lithostatic pressure) and ductile flow of olivine [*Brace and Kohlstedt*, 1980]. The black dashed line is the strength envelope for hydrostatic case ($\lambda = 0.4$). The red dashed line is the maximum slip versus depth for the L2 norm regularization approach in Figure 2c, and the red solid line is that for the sparse regularization approach in Figure 2d. (b) Histogram of 1 month aftershock depth from double-difference hypocenter solutions (F. Waldhauser, personal communication, 2014). (c) Schematic diagram of the subduction zone near the epicenter of the earthquake. The vertical scale is approximately the same as Figures 4a and 4b. The white line in the mantle is the 600°C isotherm that separates the brittle and ductile mantle.

Tests show that forward modeling based on *Montési* [2004] is not sensitive to the shear zone thickness because it trades off with the coefficient *A* (a rheological material constant; see equations in Table 1 in *Montési* [2004]). Wider shear zone thickness will result in smaller *A* but have no effect on the final displacement. However, the modeled displacement history is sensitive to the background (pre-earthquake) slip rate of the shear zone. If the background slip rate is 1 cm/yr and then subjected to a 1 MPa (L2 model) or 5–10 MPa (sparse Model) coseismic stress change, forward modeling shows that the ambient stress in the shear zone needs to be larger than 5 MPa (L2) or 25–50 MPa (sparse) to be consistent with the lack of a postseismic signal (Figure 3). However, if slip rate is 1 mm/yr, the ambient stress only needs to be larger than 0.5 MPa (L2) or 2.5–5 MPa (sparse). In both cases, this constraint is consistent with the strength envelope at 30 km depth. In contrast, the ambient stress level in the shear zone at plate boundaries might be as small as the coseismic stress perturbation [*Montési*, 2004].

5. Discussion

We calculated a strength envelope for the subducting lithosphere at the location of the 2010 M_w 6.5 earthquake (Figure 4). We assumed a friction coefficient of 0.6 and a layered density model to calculate the brittle strength envelope following the expressions for a strike-slip fault in *Zoback and Townend* [2001] for both the dry and hydrostatic fluid pressure cases. The density structure beneath the seafloor includes 2 km of sediment, 5 km of continental crust, and 6 km of oceanic crust [*Blair et al.*, 2011]. Below the oceanic crust lies the oceanic mantle. We calculated a thermal model for the subducting mantle using a half-space cooling model for a 10 Ma year old oceanic plate as is expected for the 2010 earthquake based on a spreading rate of 2.5 cm/yr for the Gorda Ridge. As a simplistic attempt to account for the burial of the oceanic plate beneath the overriding plate, this thermal model is shifted in depth by 7 km. A strain rate of 10^{-14} yr^{-1} is used [*Burgmann and Dresen*, 2008]. For the ductile region, we use a power law creep relationship to calculate the differential stress [*Brace and Kohlstedt*, 1980]. We combine the brittle and diffusion creep strength estimates for an overall strength estimate following *Roland et al.* [2010]. The peak of the dry strength envelope occurs at ~600 MPa in the 15–25 km depth range where both the coseismic slip and the aftershocks are concentrated (Figure 4). Thus, the earthquake ruptured through the strongest portion of the lithosphere. The correspondence between the slip distribution and the strength envelope resembles the results for the 2012

M_w 8.6 Wharton basin earthquakes off-Sumatra [*Wei et al.*, 2013]. While this agreement with the peak depth of the strength envelope corroborates the inference of a high stress level from the apparent stress estimate, the exact stress level is uncertain due to the unknown fluid pressure (Figure 4). Even the hydrostatic stress envelope in the 15–25 km depth range (~300 MPa) is somewhat larger than what the apparent stress measurement predicts for the stress level (~7 MPa = >~120 MPa) according to the relationship in *Choy and McGarr* [2002]. This discrepancy may simply result from the uncertainty in the apparent stress measurement as other Gorda plate events have higher apparent stress.

The relationship between ambient stress S and the static stress drop $\Delta\sigma$ in earthquakes is one of the largest uncertainties in earthquake physics. High-resolution studies support the overall inference that static stress drops increase with depth in the crust and possibly with focal mechanism type as one would expect from a dependence of $\Delta\sigma$ on S [*Hardebeck and Aron*, 2009]. However, the exact ratio $\Delta\sigma/S$ is difficult to constrain because the ambient stress level is not easily measured. The 2010 earthquake is an unusually good candidate to constrain this ratio because it occurs close to the brittle-ductile transition in an olivine-dominated fault system, and the rheology of olivine in this depth range, represented by the strength envelope, is well constrained from laboratory experiments. While the oceanic mantle is thought to be initially dry after proceeding through the melting zone at the ridge, it is possible that strength is somewhat reduced due to fluid infiltration in the downgoing plate. Thus, the average strength in the 2010 rupture zone is likely in the 300–600 MPa range depending on the effect of fluid infiltration. Combining this value with the range of static stress drop estimates consistent with the GPS displacements (~20 MPa) leads to a value of $\Delta\sigma/S$ that is on the order of 0.05. Even with a factor of ~5 uncertainty from the various calculations involved in that estimate, it remains indicative of ordinary frictional sliding. It is similar to the values around 0.05 found by numerous laboratory studies that have constrained the pressure dependence of stress drop during ordinary frictional sliding [*Beeler et al.*, 2012].

The small ratio of $\Delta\sigma/S$ is surprising because the 2010 event occurs in a regime where significant dynamic weakening is expected. High-speed friction experiments on peridotite by *Del Gaudio et al.* [2009] suggest that melting is unavoidable at the stress levels expected at the depth of the peak slip and that the melting would produce a very large drop in strength for even small amounts of slip [*Del Gaudio et al.*, 2009]. In those experiments the friction coefficient drops from an ordinary 0.6 to less than 0.2 over an amount of slip known as the "thermal slip distance." Microstructural analysis indicates that this drop is due to local melting of the rock [*Del Gaudio et al.*, 2009]. The thermal slip distance is a strong function of normal stress, such that at normal mantle conditions, the transition to friction <0.2 should be "easily achieved after a few tens of centimeters (of slip) or less" [*Del Gaudio et al.*, 2009]. Thus, if both the strength envelope and the rock mechanics experiments hold, we could plausibly see dynamic stress drops of ~(0.6–0.2) × strength = ~200 MPa for the 2010 earthquake. If these large dynamic stress drops occurred, they should be reflected in the ratio of the apparent stress to the static stress drop, which is known as η_{SW}, the Savage and Wood efficiency [*Savage and Wood*, 1971; *Beeler et al.*, 2003]. For the 2010 earthquake the average values of apparent stress (7 MPa) and static stress drop (20 MPa) give $\eta_{SW} \approx 0.3$. This value indicates a small positive overshoot (e.g., dynamic stress greater than final stress) consistent with frictional sliding and is well below the values expected for frictional melting ($\eta_{SW} \approx 1.0$) [*Beeler et al.*, 2003].

6. Conclusion

Coseismic slip inversion of GPS observations show that the 2010 M_w 6.5 earthquake ruptured through the strongest part of the oceanic lithosphere well into the mantle. Despite the clear coseismic offsets, the PBO GPS observations show very little postseismic signal indicating that if there is a shear zone beneath the coseismic rupture, it must operate at ambient stress levels greater than 50 MPa to satisfy the lack of postseismic deformation. Strength envelopes indicate that the stress in the main shock rupture zone is probably about 300–600 MPa, yet the average static stress drop of this earthquake is ordinary, ~2–20 MPa. Such a small stress drop is somewhat unexpected given the stress levels at these depths and laboratory experiments on peridotite that predicts significant dynamic weakening at these conditions due to frictional melting. Instead, our observations of the ratio of static stress drop to applied stress are consistent with ordinary frictional sliding as is the estimated ratio of apparent stress to static stress drop. This lack of direct observational evidence for weakening indicates that either oceanic lithosphere is much weaker than typical strength envelopes suggest or more likely that the conditions necessary for dynamic weakening are not yet easily extrapolated to specific tectonic environments even for the relatively homogenous case of oceanic upper mantle.

References

Anderson, G. (2004), *Plate Boundary Observatory Data Management Plan*, UNAVCO, Boulder, Colo.

Beeler, N. M., T. F. Wong, and S. H. Hickman (2003), On the expected relationships among apparent stress, static stress drop, effective shear fracture energy, and efficiency, *Bull. Seismol. Soc. Amer.*, *93*(3), 1381–1389.

Beeler, N., B. Kilgore, A. McGarr, J. Fletcher, J. Evans, and S. R. Baker (2012), Observed source parameters for dynamic rupture with non-uniform initial stress and relatively high fracture energy, *J. Struct. Geol.*, *V38*, 77–89.

Blair, J. L., P. A. McCrory, D. H. Oppenheimer, and F. Waldhauser (2011), A geo-referenced 3D model of the Juan de Fuca slab and associated seismicity, *USGS Survey Data Series* 633, v.1.2. [Available at http://pubs.usgs.gov/ds/633/.]

Brace, W. F., and D. L. Kohlstedt (1980), Limits on lithospheric stress imposed by laboratory experiments, *J. Geophys. Res.*, *85*(B11), 6248–6252, doi:10.1029/JB085iB11p06248.

Burgmann, R., and G. Dresen (2008), Rheology of the lower crust and upper mantle: Evidence from rock mechanics, geodesy, and field observations, *Annu. Rev. Earth Planet. Sci.*, *36*(1), 531–567, doi:10.1146/annurev.earth.36.031207.124326.

Chaytor, J. D., C. Goldfinger, R. P. Dziak, and C. G. Fox (2004), Active deformation of the Gorda plate: Constraining deformation models with new geophysical data, *Geology*, *32*, 353–356, doi:10.1130/G20178.2.

Choy, G. L., and A. McGarr (2002), Strike-slip earthquakes in the oceanic lithosphere: Observations of exceptionally high apparent stress, *Geophys. J. Int.*, *150*(2), 506–523, doi:10.1046/j.1365-246X.2002.01720.x.

Del Gaudio, P., G. Di Toro, R. Han, T. Hirose, S. Nielsen, T. Shimamoto, and A. Cavallo (2009), Frictional melting of peridotite and seismic slip, *J. Geophys. Res.*, *114*, B06306, doi:10.1029/2008JB005990.

Dziewonski, A. M., and D. L. Anderson (1981), Preliminary Reference Earth Model (PREM), *Phys. Earth Planet. Inter.*, *25*, 297–356.

Evans, E. L., and B. J. Meade (2012), Geodetic imaging of coseismic slip and postseismic afterslip: Sparsity promoting methods applied to the great Tohoku earthquake, *Geophys. Res. Lett.*, *39*, L11314, doi:10.1029/2012GL051990.

Fialko, Y., D. Sandwell, M. Simons, and P. Rosen (2005), Three-dimensional deformation caused by the Bam, Iran, earthquake and the origin of shallow slip deficit, *Nature*, *435*, 295–299, doi:10.1038/nature03425.

Freed, A. M. (2007), Afterslip (and only afterslip) following the 2004 Parkfield, California, earthquake, *Geophys. Res. Lett.*, *34*, L06312, doi:10.1029/2006GL029155.

Hardebeck, J. L., and A. Aron (2009), Earthquake stress drops and inferred fault strength on the Hayward Fault, East San Francisco Bay, California, *Bull. Seismol. Soc. Am.*, *99*(3), 1801–1814, doi:10.1785/0120080242.

Herring, T. A. (2006), SNARF realization for PBO processing, presentation given at the 5th SNARF Workshop, Denver, Colo., 15 Mar.

Hsu, Y.-J., M. Simons, J.-P. Avouac, J. Galetzka, K. Sieh, M. Chlieh, D. Natawidjaja, L. Prawirodirdjo, and Y. Bock (2006), Frictional afterslip following the 2005 Nias-Simeulue earthquake, Sumatra, *Science*, *312*, 1921–1926, doi:10.1126/science.1126960.

McGuire, J. J., and P. Segall (2003), Imaging of aseismic fault slip transients recorded by dense geodetic networks, *Geophys. J. Int.*, *155*, 778–788, doi:10.1111/j.1365-246X.2003.02022.x.

Montési, L. G. J. (2004), Controls of shear zone rheology and tectonic loading on postseismic creep, *J. Geophys. Res.*, *109*, B10404, doi:10.1029/2003JB002925.

Murray, J. R., P. Segall, P. Cervelli, W. Prescott, and J. Svarc (2001), Inversion of GPS data for spatially variable slip-rate on the San Andreas Fault near Parkfield, CA, *Geophys. Res. Lett.*, *28*(2), 359–362, doi:10.1029/2000GL011933.

Ohtani, R., J. J. McGuire, and P. Segall (2010), Network strain filter: A new tool for monitoring and detecting transient deformation signals in GPS arrays, *J. Geophys. Res.*, *115*, B12418, doi:10.1029/2010JB007442.

Okada, Y. (1985), Surface deformation due to shear and tensile faults in a half-space, *Bull. Seismol. Soc. Am.*, *75*(4), 1135–1154, doi:10.1016/0148-9062(86)90674-1.

Ripperger, J., and P. M. Mai (2004), Fast computation of static stress changes on 2D faults from final slip distributions, *Geophys. Res. Lett.*, *31*, L18610, doi:10.1029/2004GL020594.

Roland, E., M. D. Behn, and G. Hirth (2010), Thermal-mechanical behavior of oceanic transform faults: Implications for the spatial distribution of seismicity, *Geochem. Geophys. Geosyst.*, *11*, Q07001, doi:10.1029/2010GC003034.

Rollins, J. C., and R. S. Stein (2010), Coulomb stress interactions among M ≥ 5.9 earthquakes in the Gorda deformation zone and on the Mendocino Fault Zone, Cascadia subduction zone, and northern San Andreas Fault, *J. Geophys. Res.*, *115*, B12306, doi:10.1029/2009JB007117.

Savage, J. C., and M. D. Wood (1971), Relation between apparent stress and stress drop, *Bull. Seismol. Soc. Amer.*, *61*(5), 1381–1388.

Segall, P., and M. Matthews (1997), Time dependent inversion of geodetic data, *J. Geophys. Res.*, *102*, 22,391–22,409, doi:10.1029/97JB01795.

Wei, M., J. J. McGuire, and E. Richardson (2012), A slow slip event in the south central Alaska Subduction Zone and related seismicity anomaly, *Geophys. Res. Lett.*, *39*, L15309, doi:10.1029/2012GL052351.

Wei, S., D. Helmberger, and J.-P. Avouac (2013), Modeling the 2012 Wharton basin earthquakes off-Sumatra: Complete lithospheric failure, *J. Geophys. Res. Solid Earth*, *118*, 3592–3609, doi:10.1002/jgrb.50267.

Wilson, D. S. (1986), A kinematic model for the Gorda Deformation Zone as a diffuse southern boundary of the Juan de Fuca Plate, *J. Geophys. Res.*, *91*, 10,259–10,269, doi:10.1029/JB091iB10p10259.

Zoback, M., and J. Townend (2001), Implications of hydrostatic pore pressures and high crustal strength for the deformation of intraplate lithosphere, *Tectonophysics*, *336*, 19–30, doi:10.1016/S0040-1951(01)00091-9.